

Non-Fermi liquid behaviour in a correlated flat-band pyrochlore lattice

Received: 29 April 2023

Accepted: 29 November 2023

Published online: 26 January 2024

 Check for updates

Jianwei Huang¹, Lei Chen^{1,6}, Yuefei Huang^{2,6}, Chandan Setty^{1,6}, Bin Gao¹, Yue Shi³, Zhaoyu Liu³, Yichen Zhang¹, Turgut Yilmaz⁴, Elio Vescovo⁴, Makoto Hashimoto⁵, Donghui Lu⁵, Boris I. Yakobson², Pengcheng Dai¹, Jiun-Haw Chu³, Qimiao Si¹✉ & Ming Yi¹✉

Electronic correlation effects are manifested in quantum materials when either the on-site Coulomb repulsion is large or the electron kinetic energy is small. The former is the dominant effect in cuprate superconductors and heavy-fermion systems whereas it is the latter in twisted bilayer graphene and geometrically frustrated metals. However, the simultaneous cooperation of both effects in the same quantum material remains rare. The design aim is to produce correlated topological flat bands pinned at the Fermi level. Here, we observe a flat band at the Fermi level in a 3*d* pyrochlore metal CuV₂S₄. Our angle-resolved photoemission spectroscopy data reveal that destructive quantum interference associated with the V pyrochlore sublattice and further renormalization to the Fermi level by electron interactions induce this flat band. Consequently, we discover transport signatures that evidence a deviation from Fermi liquid behaviour as well as an enhanced Sommerfeld coefficient. Our work illustrates the combined cooperation of local Coulomb interactions and geometric frustration in a pyrochlore lattice system to induce correlated topology by constructing and pinning correlated flat bands near the Fermi level.

Quantum many-body effects are manifested in materials in which the electron kinetic energy (t) is small or comparable to the on-site Coulomb interactions (U)¹, $U/t \geq 1$, leading to spontaneous symmetry-breaking orders such as magnetism, nematicity, unconventional superconductivity and charge density waves (CDWs)^{2–5}. Such a regime can be reached either in materials with strong Coulomb interactions (large U), such as cuprates, iron-based superconductors and heavy-fermion systems, or in materials with quenched kinetic energies (small t) through the construction of flat bands in a moiré superlattice or through destructive quantum interference^{6–11}. In the former case, the electrons feel the strong repulsion from the nearby electrons and cannot be treated simply as single particles. As a result, the electron mass is strongly enhanced and the band velocity strongly renormalized, which often

lead to non-Fermi liquid transport and quantum criticality and can sometimes reach the limit of Mott insulating phases^{2,4,12–16}. In the latter case, a quasi-flat band with small bandwidth can be achieved, for example, in twisted bilayer graphene by folding of the large moiré superlattice⁶. Similar strong correlation phenomena, including unconventional superconductivity, ferromagnetism and linear resistivity^{7,17,18}, have also been found. Alternatively, another way to realize topological flat bands is with quantum interference of the electronic wavefunction in geometrically frustrated lattices^{8,19–22}. In both twisted bilayer graphene and geometrically frustrated lattices, the non-local construction of the flat bands also deem these systems to be topological. In contrast to twisted bilayer graphene, for which devices are limited to certain experimental probes, geometrically frustrated lattices are found in

¹Department of Physics and Astronomy, Rice University, Houston, TX, USA. ²Department of Materials Science and NanoEngineering, Rice University, Houston, TX, USA. ³Department of Physics, University of Washington, Seattle, WA, USA. ⁴National Synchrotron Light Source II, Brookhaven National Lab, Upton, NY, USA. ⁵Stanford Synchrotron Radiation Lightsource, SLAC National Accelerator Laboratory, Menlo Park, CA, USA. ⁶These authors contributed equally: Lei Chen, Yuefei Huang, Chandan Setty. ✉e-mail: qmsi@rice.edu; mingyi@rice.edu

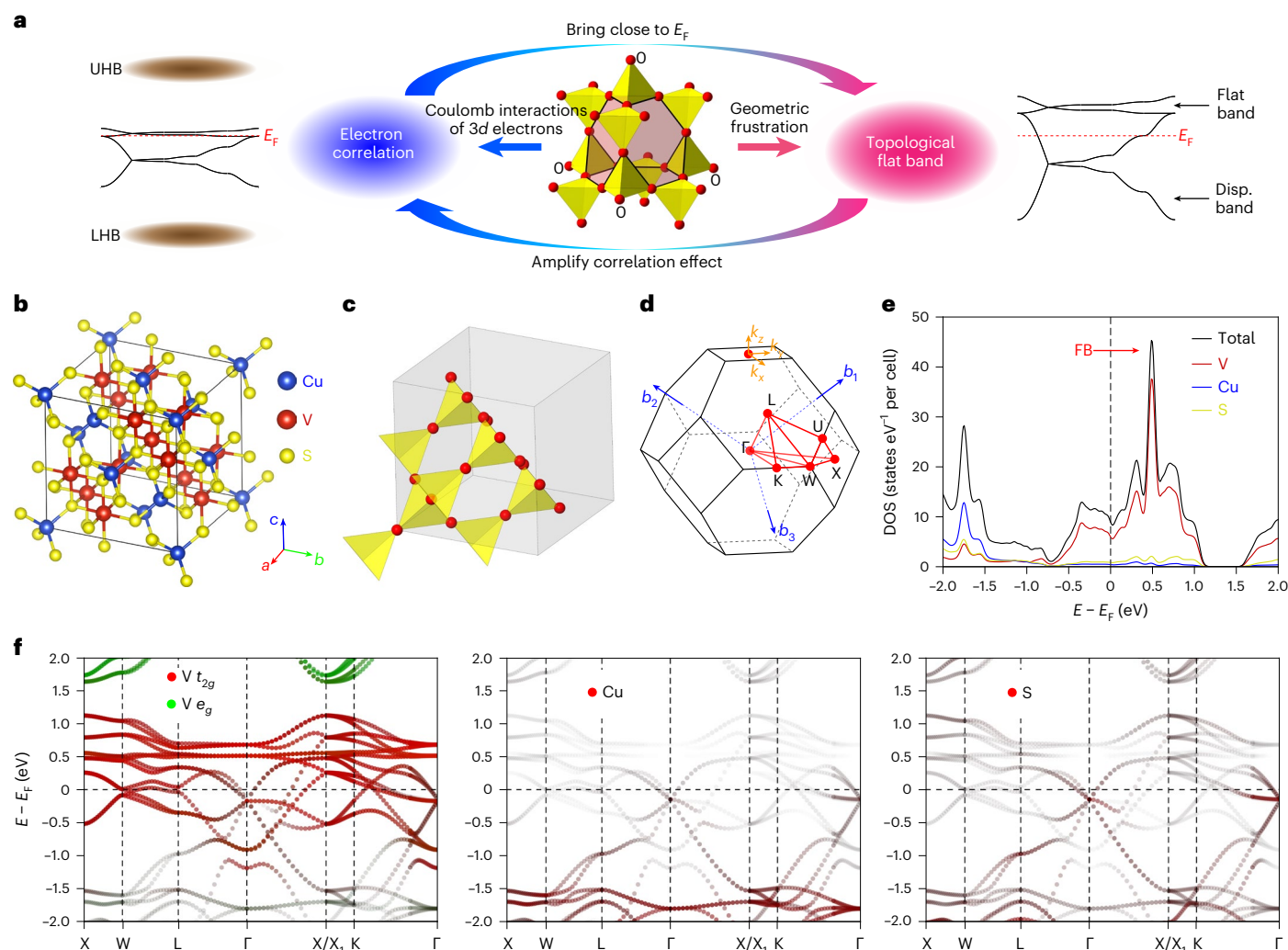


Fig. 1 | Crystal structure and DFT calculations of CuV_2S_4 . **a**, Correlation and 3D flat band in a pyrochlore lattice. The electrons are confined to the shaded region of the centre of the pyrochlore lattice, with quenched effective hopping outside the region, leading to the 3D topological flat band. Moderate correlations of 3d orbitals renormalize the topological flat band induced by 3D quantum interference so that it is close to E_F , which in turn amplifies the effects of the correlation. **b**, Crystal structure of CuV_2S_4 . The V atoms are surrounded by the S tetrahedron, and the Cu atoms are surrounded by the S octahedron. **c**, The

atoms form a pyrochlore sublattice, which consists of corner-sharing tetrahedra. **d**, The 3D Brillouin zone, with the corresponding high-symmetry points labelled. The blue arrows mark the primitive unit cell basis vectors. The yellow arrows mark the ARPES measurement coordinates. **e**, DOS and projected DOS from DFT calculations. The sharp peak at 0.5 eV indicates the 3D flat band (FB). **f**, Band dispersion of CuV_2S_4 , projected onto the $V t_{2g}$ and e_g orbitals and Cu and S atoms from DFT calculations. disp., dispersive; LHB, lower Hubbard band; UHB, upper Hubbard band.

a wide range of materials for which large high-quality single crystals are available^{23–25}.

An optimal way to enhance U/t is, therefore, to have both large U and small t by combining the two methods such that electron–electron interactions are strong in a system that exhibits natural flat bands due to destructive quantum interference. Although flat bands have been theoretically predicted and experimentally identified in kagome materials, when realized in bulk, the finite interlayer coupling disrupts the in-plane quantum interference, often leading to a relatively large bandwidth^{23–26}. To find an optimal geometrically frustrated lattice, we seek materials that belong to the three-dimensional (3D) analogue, the pyrochlore lattice^{27–29}. Although numerous crystal structural families feature a pyrochlore sublattice, including traditional pyrochlores, Laves phases and spinels, a metallic compound characterized by minimal hybridization between the electronic states arising from the constituents of the pyrochlore sublattice and those of the other atomic sites is particularly conducive to the formation of a flat band³⁰. In this context, the spinel CuV_2S_4 emerges as a highly promising candidate³¹.

By using a combination of angle-resolved photoemission spectroscopy (ARPES), first-principles calculations, auxiliary-spin calculations, and transport and thermodynamic measurements, we identify a topological flat band near the Fermi level that is induced by the combined effect of the pyrochlore lattice geometry and on-site Coulomb interactions (Fig. 1a). This is consistent with our observation of non-Fermi liquid transport and a large Sommerfeld coefficient in CuV_2S_4 . Our study reveals a cooperative mechanism between the quantum-interference topological flat band and local Coulomb interactions, and it lays the foundation for identifying model bulk systems for emergent phases in strongly correlated topological systems.

CuV_2S_4 is a face-centred cubic material that forms in the space group of $Fd\bar{3}m$ (Fig. 1b)^{32,33}. The Cu atoms form a diamond sublattice and the V atoms form a pyrochlore sublattice (Fig. 1c). Importantly, the pyrochlore lattice is a geometrically frustrated lattice in which destructive 3D quantum interference confines the electron wavefunction to the centre of the 3D block surrounded by the tetrahedra (Fig. 1a), leading to 3D flat bands in momentum space^{27–29}. This mechanism can be understood more

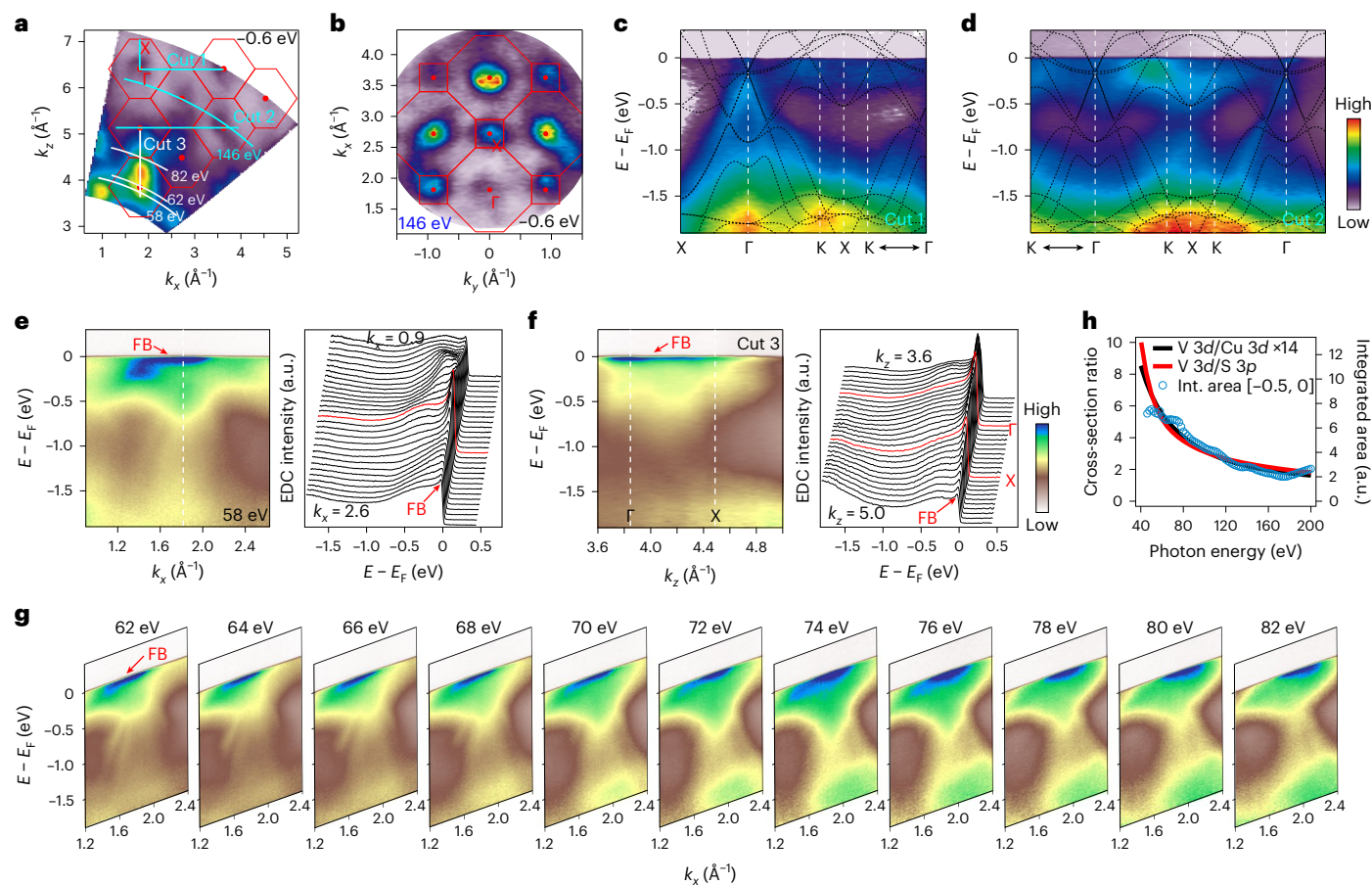


Fig. 2 | Electronic structure and 3D flat band of CuV_2S_4 by ARPES. **a**, Out-of-plane constant-energy contour mapping at -0.6 eV measured for different photon energies with respect to the (001) surface. The red solid lines mark the corresponding Brillouin zone. The cyan and white solid lines mark the cut positions. **b**, In-plane constant-energy contour mapping at -0.6 eV of the (001) surface. **c,d**, Spectral images of cut 1 (**c**) and cut 2 (**d**), as indicated in **a** with the corresponding band dispersion from the DFT calculations (black dashed lines) overlaid on top. **e**, Spectral image and corresponding EDC stacks showing the flat band around E_F measured by 58 eV photons with the corresponding momentum

position indicated in **a**. **f**, Spectral image and corresponding EDC stacks showing the flat band around E_F along the out-of-plane direction as indicated in **a**. **g**, Spectral images measured with different photon energies showing the 3D flat band. The corresponding cut positions are indicated in **a**. **h**, Photoionization cross-section ratios of V 3d over Cu 3d and S 3p orbitals (<https://vuo.elettra.eu/services/elements/WebElements.html>) and integrated spectral weight of the EDCs in **f** over the energy range of -0.5 – 0 eV as a function of the incident photon energy. a.u., arbitrary units; Int., integrated.

intuitively by considering the pyrochlore lattice as alternately stacked kagome lattices and triangular lattices along the (111) direction with the interlayer coupling being completely quenched^{29,30}. From our density-functional theory (DFT) calculations of CuV_2S_4 (Fig. 1e,f), the electronic states near the Fermi level are dominated by the V 3d orbitals whereas the contributions from Cu and S atoms are mainly 1 eV below E_F . Notably, there is a sharp peak in the density of states (DOS) 0.5 eV above E_F (Fig. 1e). This sharp peak indicates the 3D quantum-interference-induced flat bands, as further revealed by the calculated band dispersions (Fig. 1f)^{27–29}. This calculation is consistent with the independent calculation in the materials database²⁰. We demonstrate that the flat band's origin is the destructive quantum interference, as evidenced by the absence of the flat band in an artificially distorted lattice of CuV_2S_4 after purposely disrupting the pyrochlore lattice (Supplementary Fig. 10). As the low-energy electronic states are dominated by the V atoms with negligible hybridization to the Cu and S states, the pyrochlore physics is expected to be manifested in this compound, leading to flat bands that are topologically nontrivial^{28,29}. Note that previous studies have revealed two CDW transitions in CuV_2S_4 at around 50 and 90 K with an accompanied structural transition from cubic to orthorhombic^{34–36}, which are also consistently reproduced by our transport studies (Supplementary Fig. 1). However, the lattice distortion is very small (less than 0.05% for *a* and *b*

and less than 0.2% for *c*; ref. 36), and we did not find any dramatic modification of the electronic structure, either in the ARPES measurements or the DFT calculations (Supplementary Figs. 2, 3 and 4). Therefore, for simplicity, we focus our discussions on the cubic structure for the rest of the paper, which will not affect our conclusions.

Having revealed theoretically the existence of 3D flat bands due to geometric frustration, we next present the ARPES results. Figure 2a shows the out-of-plane constant-energy contour mapping of CuV_2S_4 at -0.6 eV with respect to the (001) surface. The corresponding in-plane mapping at -0.6 eV is shown in Fig. 2b using 146 eV photons. Both mappings exhibit a spectral intensity that matches well with the Brillouin zone periodicity. From these, we are able to obtain precise cuts along the high-symmetry momentum directions (Fig. 2c,d). Overall, the measured spectral images match well with the calculated band dispersions below -0.5 eV, where the DOS is largely dominated by the Cu and S orbitals, which is consistent with a previous photoemission study³⁷. Near E_F , however, the measured electronic structure exhibits moderate deviations from DFT calculations. Surprisingly, we observe a flat band near the Fermi level. Its intensity is more strongly manifested when measured at smaller photon energies. An example of this is shown along the momentum cut indicated in Fig. 2a as measured by 58 eV photons (Fig. 2e). To examine the flat band around E_F more closely, we plot the

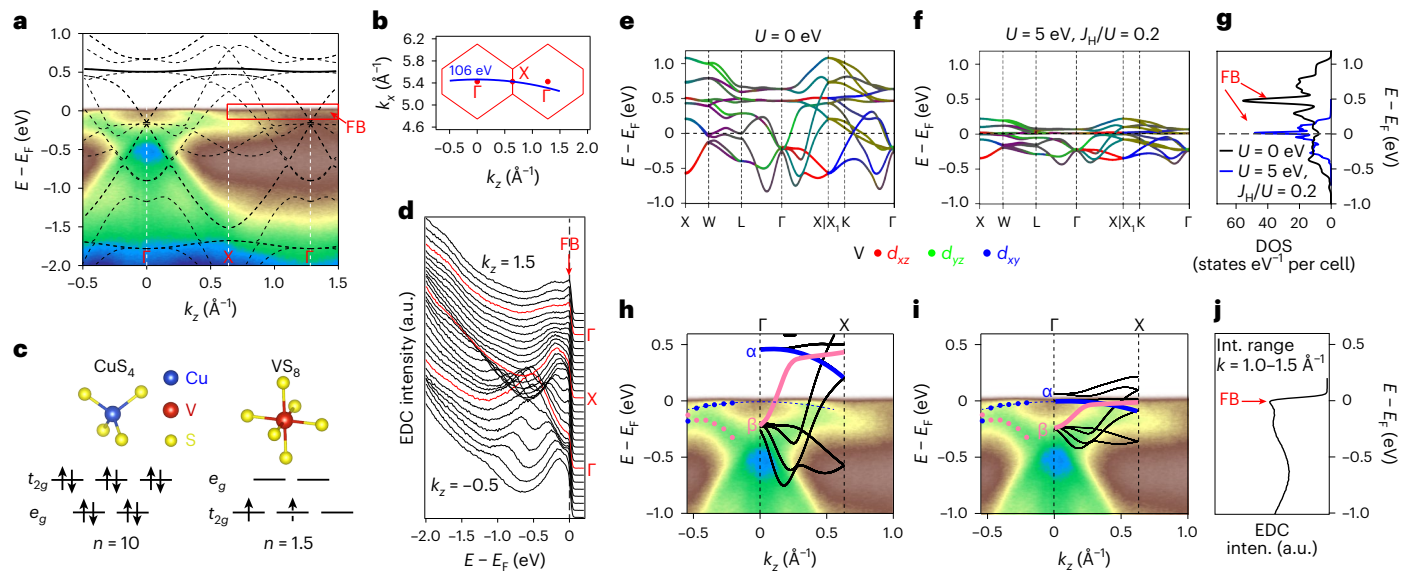


Fig. 3 | Electron correlation effects and the flat band at E_F . **a**, Spectral image measured on the (110) surface with the corresponding DFT calculations overlaid. Data taken at 106 eV. The solid line is the flat band at around 0.5 eV by calculations. The red arrow points to the measured flat band around E_F . **b**, Brillouin zone and the momentum cut position of **a**. **c**, The crystal field splitting and electron filling of 3d orbitals of Cu and V atoms. The Cu 3d orbitals are completely filled by ten electrons. The three V t_{2g} orbitals are filled by an average of 1.5 electrons. **d**, EDC stacks of the spectral image in **a**. The red arrow marks the flat band around E_F . **e**, The band dispersion for the 12-band model by auxiliary-spin calculations without including electron correlations ($U = 0$ eV and

$J_H = 0$ eV). **f**, Same as **e** but including electron correlations ($U = 5$ eV and $J_H/U = 0.2$). **g**, DOS of band dispersion by the auxiliary-spin calculations. **h**, Comparison of the spectral image from ARPES and auxiliary-spin calculations (overlaid solid lines) with $U = 0$ eV along the Γ -X direction. The blue and pink solid circles are fitted band dispersions, which match with the blue (α) and pink (β) solid lines from the calculated bands. The blue dashed line is a quadratic fit of the α band (blue solid circles), which gives a band top at -7 meV. **i**, Same as **h** but with $U = 5$ eV and $J_H/U = 0.2$. **j**, Integrated EDC of the spectral image in **a** showing the flat-band peak around E_F . arb., arbitrary; Inten., intensity.

stack of energy distribution curves (EDCs) for the corresponding spectral image. The sharp peaks in the EDCs marked by the red arrow confirm the flat band around E_F . Next, we examine this flat feature along the out-of-plane direction (Fig. 2f). Sharp peaks are also observed at E_F in the corresponding EDC stack. This is further illustrated by the series of spectral images measured with different photon energies (Fig. 2g). The flat band spans almost the entire Brillouin zone, thus revealing its 3D nature. Moreover, the stronger flat-band intensity with relatively lower photon energies is consistent with it having a dominantly V 3d orbital character, as the expected photoionization cross-section ratios of the V 3d over Cu 3d and S 3p orbitals (<https://vuo.elettra.eu/services/elements/WebElements.html>) increases as the photon energy decreases in the range of photon energies that we experimentally probed (Fig. 2h and Supplementary Fig. 6).

Although both our DFT calculations and ARPES measurements revealed the existence of a 3D flat band in CuV_2S_4 , these two flat bands are in different energy positions. The flat band predicted by the DFT calculations is 0.5 eV above the Fermi level whereas it is observed to be located at E_F experimentally (Fig. 3a). This disagreement is not only limited to the flat band but also other bands in the near- E_F region, suggesting that the V 3d-dominated bands may exhibit non-negligible electron correlation effects. Note that for CuV_2S_4 , each Cu atom is surrounded by S atoms forming a tetrahedron whereas each V atom is surrounded by S atoms forming an octahedron (Fig. 3c). As a result, the 3d orbitals of Cu are split into t_{2g} and e_g orbitals by the crystal field with the t_{2g} orbitals at a higher energy. The situation is reversed for the V 3d orbitals in the octahedral environment, as the e_g orbitals have a higher energy. It has been reported that the Cu 3d orbitals are fully occupied with ten electrons, which is consistent with the negligible Cu 3d states near E_F from DFT calculations (Fig. 1e,f)³⁸. For the V 3d orbitals, an average of 1.5 electrons fill the three degenerate t_{2g} orbitals, so that electron correlation effects are expected³⁹. This distinction between the V and Cu atomic environments is consistent with the observation that the fully

occupied Cu d bands away from E_F agree well with the DFT calculations whereas those for the near- E_F V d orbitals show a mismatch between DFT and measured dispersions (Figs. 2c,d and 3a and Supplementary Fig. 5). This strong orbital-dependent renormalization for CuV_2S_4 is reminiscent of the orbital selectivity of iron-based superconductors, for which electron correlation effects are strongly enhanced for the Fe d_{xy} orbital compared to other 3d orbitals^{39–45}.

To incorporate the effects of the electron correlation to the near- E_F states in the calculated electronic structure, we performed an auxiliary-spin calculation of a 12-band model comprising the V t_{2g} orbitals on the pyrochlore sublattice obtained by fitting the DFT results of CuV_2S_4 in the near- E_F region (Methods and Supplementary Figs. 7–9). The bands calculated without incorporating the Coulomb interactions clearly reproduce the DFT calculations of the V 3d bands near E_F (Fig. 3e). We consider the effect of electron correlations by including both Coulomb interactions (U) and Hund's coupling (J_H). At a combination of $U = 5$ eV and $J_H/U = 0.2$, the overall band structure exhibits a moderate band renormalization (Fig. 3f). More interestingly, the 3D flat band is shifted close to the Fermi level (Fig. 3f,g). Indeed, a comparison of the two calculations with the corresponding ARPES spectral image shows a much improved agreement for the one incorporating correlation effects (Fig. 3h,i). This improvement is not limited to the flat band around E_F but occurs also for the dispersive low-energy electronic states around Γ and X. To further compare the calculations and the dispersive bands, we obtain the band dispersions of a hole-like α band and an electron-like β band from EDC fitting (Fig. 3h–i). Their band velocities match much better with the calculations at $U = 5$ eV and $J_H/U = 0.2$. Moreover, the band top of the α band touches the flat band, forming a quadratic band touching at Γ (ref. 46). Taking advantage of this, we estimate the energy position of the flat band by fitting the α band dispersion from experiments. The fitted band top is at -7 meV (Fig. 3h–i). Considering a tiny gap (7 meV from DFT) opening at the point Γ in the orthorhombic phase (Supplementary Fig. 2), the flat

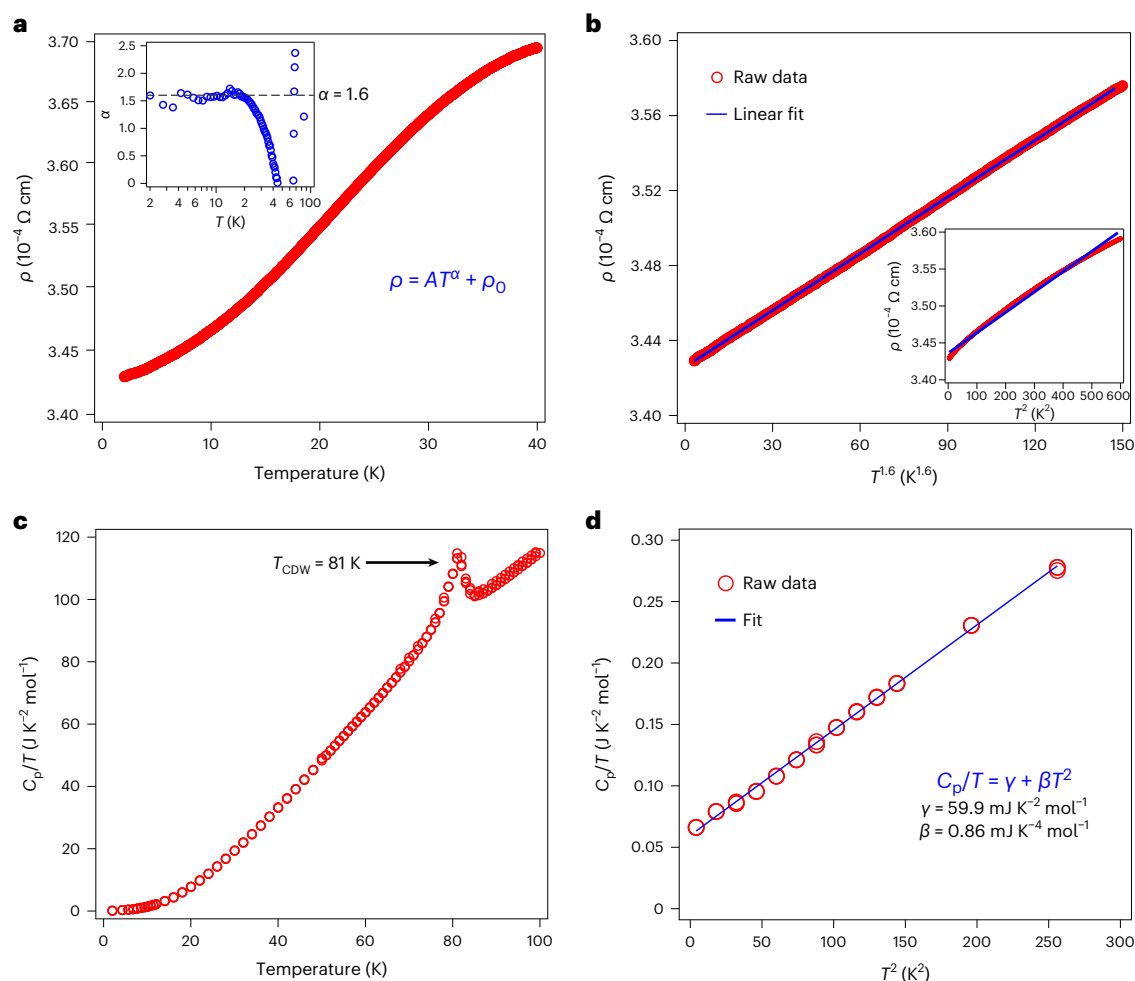


Fig. 4 | Transport and thermodynamic measurements showing the non-Fermi liquid behaviour. **a**, Resistivity of CuV_2S_4 . The inset shows the power law exponent α of the resistivity as a function of temperature. The resistivity has a power law behaviour with $\alpha = 1.6$ up to 20 K. **b**, Low-temperature resistivity

plotted as a function of $T^{1.6}$ and a linear fit. The inset shows the resistivity plotted as a function of T^2 and a linear fit (blue solid line). **c**, Measured heat capacity of CuV_2S_4 . The black arrow points to a CDW transition at around 81 K. **d**, Linear fit of C_p/T as a function of T^2 to obtain the Sommerfeld coefficient γ .

band should be in the proximity of E_F . As the energy of the flat band at Γ is also near its band bottom (Fig. 3a), we conclude that the flat-band spectral peaks we observe around E_F are likely the tail of its spectral intensity cut off by the Fermi–Dirac function, with the true energy position slightly above E_F . This is consistent with a cut measured at high temperature divided by the Fermi–Dirac function (Supplementary Figs. 13 and 14). Hence, the consistently observed renormalization of these dispersive bands as well as the presence of the flat band at E_F further demonstrates that the origin of this renormalization is the electron correlation associated with the partially filled pyrochlore $V t_{2g}$ orbitals. We emphasize that the existence of the flat band at E_F must be the combined effect of electron correlations and destructive interference. The auxiliary-spin calculations from the starting point of the distorted CuV_2S_4 crystal structure with a destroyed pyrochlore sublattice do not produce a similar flat band at E_F , hence confirming that electron correlations alone are not sufficient to give rise to the flat band in CuV_2S_4 (Supplementary Note 6).

Combining the ARPES results and the auxiliary-spin calculations suggests that CuV_2S_4 is in a regime with large U/t , a result of both large U from the on-site Coulomb interaction and small t from quantum interference associated with the pyrochlore lattice. For materials in the large U/t regime, such as unconventional superconductors and heavy-fermion compounds, the transport behaviour often deviates from a Fermi liquid^{13,47}. We, therefore, examined the transport

properties of CuV_2S_4 . Interestingly, the temperature-dependent resistivity shows a power law behaviour, $\rho(T) \propto T^\alpha$. To determine the exponent α , we plot $\alpha = \partial \ln(\rho(T) - \rho_0) / \partial \ln(T)$ as a function of temperature (inset of Fig. 4a), which shows that $\alpha = 1.6$ extending from the lowest temperature of 2 K up to 20 K (see also Supplementary Fig. 11). This is further evident in the much more linear behaviour of the resistivity plotted as a function of $T^{1.6}$ compared to the plot as a function of T^2 (Fig. 4b). This $T^{1.6}$ power law behaviour suggests non-Fermi liquid behaviour in CuV_2S_4 , which is further indicated by the non-saturating magnetic susceptibility that follows the logarithmic temperature dependence at low temperatures (Supplementary Fig. 12). Moreover, we also measured the specific heat, from which we determined the Sommerfeld coefficient, $\gamma = 60$ $mJ K^{-2} mol^{-1}$ (Fig. 4d). Notably, this γ is 6 times larger than that predicted by the DFT calculations ($\gamma_{DFT} = 10$ $mJ K^{-2} mol^{-1}$), consistent with previous reports^{48,49}. Given that this value was experimentally determined for the CDW ordered state where the DOS develops a CDW gap (Fig. 4c), this enhancement factor is likely a lower bound of the true factor and indicates the contribution from electron–electron correlations and the renormalized flat band near E_F . With that said, also note that the specific heat may not be as good a measure of the non-Fermi liquid behaviour as transport due to the potential gapping of the Fermi surface in the CDW phase, whereas the resistivity derives from the remnants of the Fermi surface and its temperature dependence captures the non-Fermi liquid property.

We now suggest a mechanism for the non-Fermi liquid behaviour based on magnetic frustration. Intuitively, flat bands could be represented in real space by molecular orbitals that are essentially localized. Such a mapping has recently been suggested for a simpler variant of the lattice with a flat band^{50–52}. The topologically nontrivial flat bands need to be combined with other wide bands so that they can be represented by exponentially localized symmetry-preserving (Kramers-doublet) Wannier orbitals, with essentially localized Wannier states that predominantly come from the flat bands and more extended Wannier states that are primarily associated with the wide bands. This leads to a Kondo-lattice description, with the two sets of Wannier states acting as the analogue of the f and of the s , p and d orbitals, respectively, of the heavy-fermion materials. Importantly, in our pyrochlore case, the analogue of f moments are geometrically frustrated. This means that the mapped Kondo-lattice model is in the highly quantum fluctuating (large G) regime of the global phase diagram of the Kondo lattice⁵³, such that the analogue of the f moments can form a spin liquid and the corresponding metallic phase can be a non-Fermi liquid phase. It has been proposed that such a phase is realized in the geometrically frustrated heavy-fermion material CePdAl (ref. 54), whose electrical resistivity has a non-Fermi liquid temperature dependence $\rho \propto T^\alpha$ with an exponent α that is smaller than the 2 for a Fermi liquid. We propose that the same phase underlies the non-Fermi liquid behaviour we have observed here in CuV₂S₄.

Hence, from the combination of ARPES, DFT and auxiliary-spin calculations and from transport and heat capacity measurements, we understand CuV₂S₄ as a system in which non-Fermi liquid behaviour emerges from a cooperative result of quantum-interference-driven quenching of the electron kinetic energy and the Coulomb interactions of the $V\ 3d\ t_{2g}$ orbitals. The spectral evidence for this is a topological flat band that forms out of geometric frustration in the single-particle picture that is then renormalized and pinned to the Fermi level by Coulomb interactions. CuV₂S₄ is a beautiful example of the design principle of creating strongly correlated topological flat bands purely out of a d -electron system by the cooperative intertwinement of reducing t and increasing U . Importantly, neither effect by itself can create the observed outcome: the destructive quantum interference by itself in CuV₂S₄ produces a flat band that is too far away from E_F to affect transport behaviour; the moderate Coulomb interactions can by themselves renormalize the dispersive bands to an extent but cannot bring a large DOS to E_F . However, the renormalization of the topological flat band amplifies the correlation effects by renormalizing a large DOS to E_F , pushing the system towards a regime in which emergent phases can arise from the large degeneracy produced in the vicinity of E_F . In a larger scope, CuV₂S₄ belongs to a wider iso-structural family of spinel 124 compounds that have a pyrochlore sublattice. LiV₂O₄ is another notable example for which strong correlation effects have been reported and with the same V pyrochlore sublattice⁵⁵. The spinel 124 structural family provides a rich material platform for systematic explorations of the tuning of both Coulomb interactions and the quantum interference using charge carriers or magnetic doping. The topological nature of the bands further implies the existence of surface states that could be observed in future studies. In an even broader context, the pyrochlore lattice is one of the many geometrically frustrated lattices that host topological flat bands. Our work lays out a method for combining local Coulomb interactions and quantum interference to amplify the effects of correlation. A vast material base is yet to be explored for such constructs.

Online content

Any methods, additional references, Nature Portfolio reporting summaries, source data, extended data, supplementary information, acknowledgements, peer review information; details of author contributions and competing interests; and statements of data and code availability are available at <https://doi.org/10.1038/s41567-023-02362-3>.

References

- Wigner, E. On the interaction of electrons in metals. *Phys. Rev.* **46**, 1002–1011 (1934).
- Dagotto, E. Correlated electrons in high-temperature superconductors. *Rev. Mod. Phys.* **66**, 763–840 (1994).
- Qazilbash, M. M. et al. Electronic correlations in the iron pnictides. *Nat. Phys.* **5**, 647–650 (2009).
- Stewart, G. R. Heavy-fermion systems. *Rev. Mod. Phys.* **56**, 755–787 (1984).
- Grüner, G. The dynamics of charge-density waves. *Rev. Mod. Phys.* **60**, 1129–1181 (1988).
- Bistritzer, R. & MacDonald, A. H. Moiré bands in twisted double-layer graphene. *Proc. Natl Acad. Sci. USA* **108**, 12233–12237 (2011).
- Cao, Y. et al. Unconventional superconductivity in magic-angle graphene superlattices. *Nature* **556**, 43–50 (2018).
- Tang, E., Mei, J. W. & Wen, X. G. High-temperature fractional quantum Hall states. *Phys. Rev. Lett.* **106**, 236802 (2011).
- Ye, L. et al. A flat band-induced correlated kagome metal. Preprint at arxiv.org/abs/2106.10824 (2021).
- Song, Z.-D. & Bernevig, B. A. Magic-angle twisted bilayer graphene as a topological heavy fermion problem. *Phys. Rev. Lett.* **129**, 047601 (2022).
- Ekahana, S. A. et al. Anomalous quasiparticles in the zone center electron pocket of the kagomé ferromagnet Fe₃Sn₂. Preprint at arxiv.org/abs/2206.13750 (2022).
- Imada, M., Fujimori, A. & Tokura, Y. Metal–insulator transitions. *Rev. Mod. Phys.* **70**, 1039–1263 (1998).
- Gurvitch, M. & Fiory, A. T. Resistivity of La_{1.825}Sr_{0.175}CuO₄ and YBa₂Cu₃O₇ to 1100 K: absence of saturation and its implications. *Phys. Rev. Lett.* **59**, 1337–1340 (1987).
- Si, Q., Rabello, S., Ingersent, K. & Smith, J. L. Locally critical quantum phase transitions in strongly correlated metals. *Nature* **413**, 804–808 (2001).
- Coleman, P., Pépin, C., Si, Q. & Ramazashvili, R. How do Fermi liquids get heavy and die? *J. Phys. Condens. Matter* **13**, R723–R738 (2001).
- Senthil, T., Vojta, M. & Sachdev, S. Weak magnetism and non-Fermi liquids near heavy-fermion critical points. *Phys. Rev. B* **69**, 035111 (2004).
- Sharpe, A. L. et al. Emergent ferromagnetism near three-quarters filling in twisted bilayer graphene. *Science* **365**, 605–608 (2019).
- Polshyn, H. et al. Large linear-in-temperature resistivity in twisted bilayer graphene. *Nat. Phys.* **15**, 1011–1016 (2019).
- Henley, C. L. The ‘Coulomb phase’ in frustrated systems. *Annu. Rev. Condens. Matter Phys.* **1**, 179–210 (2010).
- Regnault, N. et al. Catalogue of flat-band stoichiometric materials. *Nature* **603**, 824–828 (2022).
- Călugăru, D. et al. General construction and topological classification of crystalline flat bands. *Nat. Phys.* **18**, 185–189 (2022).
- Neves, P. M. et al. Crystal net catalog of model flat band materials. Preprint at arxiv.org/abs/2303.02524 (2023).
- Ortiz, B. R. et al. New kagome prototype materials: discovery of KV₃Sb₅, RbV₃Sb₅, and CsV₃Sb₅. *Phys. Rev. Mater.* **3**, 094407 (2019).
- Kang, M. et al. Dirac fermions and flat bands in the ideal kagome metal FeSn. *Nat. Mater.* **19**, 163–169 (2020).
- Yin, J.-X. et al. Quantum-limit Chern topological magnetism in TbMn₆Sn₆. *Nature* **583**, 533–536 (2020).
- Kang, M. et al. Topological flat bands in frustrated kagome lattice CoSn. *Nat. Commun.* **11**, 4004 (2020).
- Bergman, D. L., Wu, C. & Balents, L. Band touching from real-space topology in frustrated hopping models. *Phys. Rev. B* **78**, 125104 (2008).

28. Guo, H. M. & Franz, M. Three-dimensional topological insulators on the pyrochlore lattice. *Phys. Rev. Lett.* **103**, 206805 (2009).
29. Huang, J. et al. Three-dimensional flat bands and Dirac cones in a pyrochlore superconductor. Preprint at arxiv.org/abs/2304.09066 (2023).
30. Gardner, J. S., Gingras, M. J. P. & Greedan, J. E. Magnetic pyrochlore oxides. *Rev. Mod. Phys.* **82**, 53–107 (2010).
31. Ghosh, P. et al. Breathing chromium spinels: a showcase for a variety of pyrochlore Heisenberg Hamiltonians. *npj Quantum Mater.* **4**, 63 (2019).
32. Hahn, H., De Lorent, C. & Harder, B. Untersuchungen über ternäre Chalkogenide. VIII. über die Struktur des CuV_2S_4 , CuCr_2S_4 , CuCr_2Se_4 und CuCr_2Te_4 . *Z. für anorganische und Allg. Chem.* **283**, 138–142 (1956).
33. Le Nagard, N., Katty, A., Collin, G., Gorochov, O. & Willig, A. Elaboration, structure cristalline et propriétés physiques (transport, susceptibilité magnétique et R.M.N.) du spinelle CuV_2S_4 . *J. Solid State Chem.* **27**, 267–277 (1979).
34. Fleming, R. M., DiSalvo, F. J., Cava, R. J. & Waszczak, J. V. Observation of charge-density waves in the cubic spinel structure CuV_2S_4 . *Phys. Rev. B* **24**, 2850–2853 (1981).
35. Okada, H., Koyama, K. & Watanabe, K. Two-step structural modulations and Fermi liquid state in spinel compound CuV_2S_4 . *J. Phys. Soc. Jpn* **73**, 3227–3230 (2004).
36. Kawaguchi, S. et al. Structural analysis of spinel compound CuV_2S_4 with incommensurate charge-density wave. *J. Phys.: Conf. Ser.* **391**, 012095 (2012).
37. Matsuno, J., Fujimori, A., Mattheiss, L. F., Endoh, R. & Nagata, S. Photoemission and band-calculation studies of the charge-density wave in CuV_2S_4 . *Phys. Rev. B* **64**, 115116 (2001).
38. Lu, Z. W. et al. Electronic structure of CuV_2S_4 . *Phys. Rev. B* **53**, 9626–9633 (1996).
39. Georges, A., de' Medici, L. & Mravlje, J. Strong correlations from Hund's coupling. *Annu. Rev. Condens. Matter Phys.* **4**, 137–178 (2013).
40. Misawa, T., Nakamura, K. & Imada, M. Ab initio evidence for strong correlation associated with Mott proximity in iron-based superconductors. *Phys. Rev. Lett.* **108**, 177007 (2012).
41. Yu, R. & Si, Q. Orbital-selective Mott phase in multiorbital models for alkaline iron selenides $\text{K}_{1-x}\text{Fe}_{2-y}\text{Se}_2$. *Phys. Rev. Lett.* **110**, 146402 (2013).
42. Yi, M. et al. Observation of temperature-induced crossover to an orbital-selective Mott phase in $\text{A}_x\text{Fe}_{2-y}\text{Se}_2$ ($\text{A}=\text{K}, \text{Rb}$) superconductors. *Phys. Rev. Lett.* **110**, 067003 (2013).
43. Yi, M. et al. Observation of universal strong orbital-dependent correlation effects in iron chalcogenides. *Nat. Commun.* **6**, 7777 (2015).
44. Yi, M., Zhang, Y., Shen, Z.-X. & Lu, D. Role of the orbital degree of freedom in iron-based superconductors. *npj Quantum Mater.* **2**, 57 (2017).
45. Huang, J. et al. Correlation-driven electronic reconstruction in $\text{FeTe}_{1-x}\text{Se}_x$. *Commun. Phys.* **5**, 29 (2022).
46. Sun, K., Yao, H., Fradkin, E. & Kivelson, S. A. Topological insulators and nematic phases from spontaneous symmetry breaking in 2D Fermi systems with a quadratic band crossing. *Phys. Rev. Lett.* **103**, 046811 (2009).
47. Butch, N. P., Jin, K., Kirshenbaum, K., Greene, R. L. & Paglione, J. Quantum critical scaling at the edge of Fermi liquid stability in a cuprate superconductor. *Proc. Natl Acad. Sci. USA* **109**, 8440–8444 (2012).
48. Hagino, T., Seki, Y., Takayanagi, S., Wada, N. & Nagata, S. Electrical-resistivity and low-temperature specific-heat measurements of single crystals of thiospinel CuV_2S_4 . *Phys. Rev. B* **49**, 6822–6828 (1994).
49. Gauzzi, A., Moutaabbid, H., Klein, Y., Loupias, G. & Hardy, V. Fermi- to non-Fermi-liquid crossover and Kondo behavior in two-dimensional $(\text{Cu}_{2/3}\text{V}_{1/3})\text{V}_2\text{S}_4$. *J. Phys. Condens. Matter* **31**, 31LT01 (2019).
50. Chen, L. et al. Metallic quantum criticality enabled by flat bands in a kagome lattice. Preprint at arxiv.org/abs/2307.09431 (2023).
51. Chen, L. et al. Emergent flat band and topological Kondo semimetal driven by orbital-selective correlations. Preprint at arxiv.org/abs/2212.08017 (2022).
52. Hu, H. & Si, Q. Coupled topological flat and wide bands: quasiparticle formation and destruction. *Sci. Adv.* **9**, eadg0028 (2023).
53. Paschen, S. & Si, Q. Quantum phases driven by strong correlations. *Nat. Rev. Phys.* **3**, 9–26 (2020).
54. Zhao, H. et al. Quantum-critical phase from frustrated magnetism in a strongly correlated metal. *Nat. Phys.* **15**, 1261–1266 (2019).
55. Kondo, S. et al. LiV_2O_4 : a heavy fermion transition metal oxide. *Phys. Rev. Lett.* **78**, 3729–3732 (1997).

Publisher's note Springer Nature remains neutral with regard to jurisdictional claims in published maps and institutional affiliations.

Springer Nature or its licensor (e.g. a society or other partner) holds exclusive rights to this article under a publishing agreement with the author(s) or other rightsholder(s); author self-archiving of the accepted manuscript version of this article is solely governed by the terms of such publishing agreement and applicable law.

© The Author(s), under exclusive licence to Springer Nature Limited 2024

Methods

Sample growth and characterization

Polycrystalline CuV_2S_4 was first prepared by a solid state method. The stoichiometric mixture of high-purity Cu (99.99%), V (99.9%) and S (99.9%) powders was ground and pressed into a pellet inside an argon glovebox. The pellet was sealed in an evacuated quartz tube and heated at 1,123 K for 1 week. The pellet was then ground again and sealed in an evacuated quartz tube with iodine as the transport agent. The tube was placed in a tube furnace for 2 weeks, with the hot end held at 1,123 K and the cold end at 1,023 K. Crystals with a maximum size of $1 \times 1 \times 1 \text{ mm}^3$ were found in the cold end.

ARPES measurements

ARPES experiments were performed at beamlines 5-2 of the Stanford Synchrotron Radiation Lightsource and the National Synchrotron Light Source II ESM beamlines of Brookhaven National Laboratory. Both beamlines were equipped with DA30 electron analysers. The results were reproduced at both facilities. The angular resolution was set to 0.1° . The total energy resolution was set to 20 meV or better. All the samples were cleaved in situ at 15 K and all the measurements were conducted in ultra-high vacuum with a base pressure lower than 5×10^{-11} Torr.

DFT calculations

All DFT calculations were performed with the Vienna ab initio simulation package (VASP) code^{56,57} using the Perdew–Burke–Ernzerhof exchange–correlation functional⁵⁸. The energy cutoff of the plane wave basis was 450 eV, and the 3D Brillouin zone was sampled with a k -point mesh of $6 \times 6 \times 6$. All atoms were relaxed until the residual force was under 0.01 eV \AA^{-1} . A tight-binding model with 12 orbitals was fitted from the DFT results with Wannier functions, as implemented in the Wannier90 package⁵⁹.

Auxiliary-spin calculations

We used the $U(1)$ auxiliary-spin method⁶⁰ to understand the effect of the correlation in CuV_2S_4 . We considered a multiorbital Hubbard model:

$$H = H_0 + H_{\text{int}}, \quad (1)$$

where

$$H_0 = \sum_{ij\alpha\beta\sigma} t_{ij}^{\alpha\beta} d_{i\alpha\sigma}^\dagger d_{j\beta\sigma} + \sum_{i\alpha\sigma} (\epsilon_\alpha - \mu) d_{i\alpha\sigma}^\dagger d_{i\alpha\sigma} \quad (2)$$

is the tight-binding model of 12 orbitals fitted from the DFT results. $d_{i\alpha\sigma}^\dagger$ is the creation operator in the i th unit cell, with σ denoting the spin and $\alpha = (o, s)$ enumerating both the orbital and sublattice indices, respectively. In the calculation, the chemical potential μ was varied to fix the total filling in each unit cell to be 6. The sum of the coherent and incoherent parts below the chemical potential was equal to 1.5 electrons per site. For the interaction part, we consider the following Hamiltonian

$$H_{\text{int}} = \sum_{i,s} \left[\frac{U}{2} \sum_{o\sigma} n_{i\sigma s o} n_{i\sigma s o} + \sum_{o<o',\sigma} \left[U' n_{i\sigma s o} n_{i\sigma' s \sigma} + (U' - J) n_{i\sigma s o} n_{i\sigma' s \sigma} - J (d_{i\sigma s o}^\dagger d_{i\sigma s \sigma} d_{i\sigma' s \sigma}^\dagger d_{i\sigma' s o} - d_{i\sigma s o}^\dagger d_{i\sigma s \sigma}^\dagger d_{i\sigma' s \sigma} d_{i\sigma' s o}^\dagger) \right] \right], \quad (3)$$

where $n = d^\dagger d$ is the density operator. U , U' and J denote the intra-orbital Hubbard interaction, interorbital repulsion and the Hund's coupling, respectively. During the simulation, we take $U' = U - 2J$. In the auxiliary-spin method, the electron creation operator $d_{i\alpha\sigma}^\dagger = S_{i\alpha\sigma}^+ f_{i\alpha\sigma}^\dagger$, where the auxiliary spin S^+ represents the charge degree of freedom. The spinon operator f carries the spin degree of freedom. The band renormalization effect is signalled by the decreasing of the orbital

resolved quasiparticle weight $Z_\alpha = |S_\alpha^+|^2$. The DOS is calculated by the integral over the single-electron spectral function with $A(\omega) = \sum_k A(k, \omega)$, where the single-electron spectral function $A(k, \omega)$ is obtained from the convolution of the auxiliary-spin and auxiliary-fermion Green's functions⁶⁰.

Data availability

All data needed to evaluate the conclusions are present in the paper and supplementary materials. Source data are provided with this paper. Additional data are available from the corresponding author on reasonable request.

Code availability

The code for the band structure calculations used in this study are available from the corresponding authors upon reasonable request.

References

- Kresse, G. & Furthmüller, J. Efficient iterative schemes for ab initio total-energy calculations using a plane-wave basis set. *Phys. Rev. B* **54**, 11169–11186 (1996).
- Kresse, G. & Joubert, D. From ultrasoft pseudopotentials to the projector augmented-wave method. *Phys. Rev. B* **59**, 1758–1775 (1999).
- Perdew, J. P., Burke, K. & Ernzerhof, M. Generalized gradient approximation made simple. *Phys. Rev. Lett.* **77**, 3865–3868 (1996).
- Pizzi, G. et al. Wannier90 as a community code: new features and applications. *J. Phys. Condens. Matter* **32**, 165902 (2020).
- Yu, R. & Si, Q. $U(1)$ slave-spin theory and its application to Mott transition in a multiorbital model for iron pnictides. *Phys. Rev. B* **86**, 085104 (2012).

Acknowledgements

This research used the resources of the Stanford Synchrotron Radiation Lightsource, SLAC National Accelerator Laboratory, which is supported by the US Department of Energy (DOE), Office of Science, Office of Basic Energy Sciences (BES; Contract No. DE-AC02-76SF00515). The ARPES work at Rice University was supported by the Gordon and Betty Moore Foundation's EPIQS Initiative (Grant No. GBMF9470 to M.Y.) and the Robert A. Welch Foundation (Grant No. C-2175 to M.Y.). Y.Z. is partially supported by the Air Force Office of Scientific Research (AFOSR; Grant No. FA9550-21-1-0343 to M.Y.). The theoretical work at Rice is primarily supported by the US DOE, BES (Award No. DE-SC0018197 to Q.S. for model building and microscopic calculations and support for L.C.), by the AFOSR (Grant No. FA9550-21-1-0356 to Q.S. for materials search and support for C.S.), by the Robert A. Welch Foundation (Grant No. C-1411 for model conceptualization to Q.S.) and by the Vannevar Bush Faculty Fellowship (Grant No. ONR-VB N00014-23-1-2870 for conceptualization to Q.S.). Computational modeling was supported by the Office of Naval Research Grant N00014-22-1-2753 (Y.H. and B.I.Y.). The single-crystal synthesis work at Rice was supported by US DOE BES under Grant No. DE-SC0012311 (P.D.) and by the Robert A. Welch Foundation (Grant No. C-1839 to P.D.). The transport and thermodynamic measurements at UW were supported by the AFOSR under Grant No. FA2386-21-1-4060 and the David Lucile Packard Foundation (J.H.C.). M.H. and D.L. acknowledge the support of the US DOE, BES, Division of Material Sciences and Engineering (Contract No. DE-AC02-76SF00515).

Author contributions

M.Y. oversaw the project. C.S. and Q.S. first proposed the compound associated with the pyrochlore lattice. Single crystals were synthesized by B.G. under the guidance of P.D. J.H., Y.Z. and M.Y. carried out the ARPES measurements with the help of D.L., M.H., T.Y. and E.V. The ARPES data were analysed by J.H. The $U(1)$ auxiliary-spin calculations were carried out by L.C., C.S. and Q.S. The DFT calculations and tight-binding model fitting were carried out by Y.H. under the guidance of B.Y.

The transport and heat capacity measurements were carried out by Y.S., Z.L. and J.C. J.H. and M.Y. wrote the paper with input from all co-authors.

Competing interests

The authors declare no competing interests.

Additional information

Supplementary information The online version contains supplementary material available at <https://doi.org/10.1038/s41567-023-02362-3>.

Correspondence and requests for materials should be addressed to Qimiao Si or Ming Yi.

Peer review information *Nature Physics* thanks Paweł Starowicz and the other, anonymous, reviewer(s) for their contribution to the peer review of this work.

Reprints and permissions information is available at www.nature.com/reprints.